Evaluation of Footprint Horizontal Geolocation Accuracy of Spaceborne Full-Waveform LiDAR Based on Digital Surface Model

Cheng Wang, Xuebo Yang, Xiaohuan Xi, Hebing Zhang, Shichao Chen, Shuwen Peng, and Xiaoxiao Zhu

***Abstract*—Spaceborne full-waveform LiDAR has shown unique advantages in measuring global surface elevation. Laser footprints generally have decimeter-level vertical accuracy, meeting the requirement of ground elevation control points. In contrast, the footprint horizontal geolocation accuracy is in the meter to ten-meter levels. Although previous researches attempted to locate the footprint horizontal coordinate based on the digital surface model (DSM), the applicability and performance of the DSM-based positioning method in evaluating the footprint geolocation accuracy should be rigorously assessed before large-scale applications. Therefore, this study practices the DSM-based footprint positioning method over several study sites with various land covers and different laser campaigns. The footprint geolocation accuracy of the ICESat/GLAS (Ice, Cloud, and land Elevation Satellite/Geoscience Laser Altimeter System), the first Earth observation full-waveform LiDAR satellite, is evaluated by the DSM-based method. Results indicate that the DSM-based positioning method is only suitable for areas with significant height features, but not applicable in areas with high spatial correlation. The derived footprint geolocation accuracy (8.19-m horizontal shifting with 4.19-m standard deviation) is relatively reliable in urban site with relatively high spatial heterogeneity. This study helps make better use of the DSM-based footprint positioning method and design calibration experiments of full-waveform LiDAR satellites.**

***Index Terms*—Digital surface model (DSM), geolocation accuracy, ICESat/GLAS, spaceborne LiDAR, waveform simulation.**

Manuscript received December 20, 2019; revised March 26, 2020; accepted April 27, 2020. Date of publication May 11, 2020; date of current version May 29, 2020. This work was supported in part by the Guangxi Natural Science Fund for Innovation Research Team under Grant 2019JJF50001 and in part by the National Natural Science Foundation of China under Grant 41871264. *(Corresponding author: Xuebo Yang.)*

Cheng Wang, Xuebo Yang, Shuwen Peng, and Xiaoxiao Zhu are with the Key Laboratory of Digital Earth Science, Aerospace Information Research Institute, Chinese Academy of Sciences, Beijing 100094, China and also with the College of Resources and Environment, University of Chinese Academy of Sciences, Beijing 100049, China (e-mail: wangcheng@radi.ac.cn; yangxb@radi.ac.cn; pengsw@radi.ac.cn; zhuxx@radi.ac.cn).

Xiaohuan Xi is with the Key Laboratory of Digital Earth Science, Aerospace Information Research Institute, Chinese Academy of Sciences, Beijing 100094, China (e-mail: xixh@radi.ac.cn).

Hebing Zhang is with the College of Surveying and Land Information Engineering, Henan Polytechnic University, Jiaozuo 454003, China (e-mail: jzitzhb@hpu.edu.cn).

Shichao Chen is with the College of Geoscience and Surveying Engineering, China University of Mining and Technology, Beijing 100083, China (e-mail: csc569712522@163.com).

Digital Object Identifier 10.1109/JSTARS.2020.2992094

I. Introduction

SURFACE elevation measurements provide fundamental geographic information for topography mapping, environmental monitoring, and earth science [1]–[3]. Common global digital elevation models (GDEMs) include Shuttle Radar Topography Mission (SRTM) DEM, Advanced Spaceborne Thermal Emission and Reflection Radiometer (ASTER) GDEM, TanDEM-X DEM, and Advanced Land Observing Satellite (ALOS) World 3D, etc. [4]–[6]. Most of these GDEMs are produced by satellite optical photogrammetry and Interferometry Synthetic Aperture Radar (InSAR). Their vertical accuracies are generally in the meter to ten-meter levels [7], [8].

Light Detection and Ranging (LiDAR) is an advanced active remote sensing technique developed in the past three decades [9], [10]. High-intensity laser pulse and high-frequency laser reception sampling ensure the quick acquisition of accurate 3-D information, making LiDAR show unique advantages in topography surveying on various land surfaces [11], [12]. Compared with airborne and terrestrial LiDARs limited by spatial coverage, spaceborne LiDAR can measure surface elevation at a near-global scale [13]. The Ice, Cloud, and land Elevation Satellite (ICESat) / Geoscience Laser Altimeter System (GLAS) launched by National Aeronautics and Space Administration (NASA) is the first Earth observation full-waveform laser altimeter, which orbited from 2003 to 2009 [14]. It emits a short duration laser pulse and digitizes the returned signals in the form of full-waveform [15]. The formed footprints are nearly round with a ∼70-m diameter and ∼170-m center-to-center separation. Due to GLAS's good performance, more spaceborne LiDAR missions were scheduled. For instance, the ICESat-2 / Advanced Topographic Laser Altimeter System with a six-beam photon-counting LiDAR system was launched in September 2018 [16]. NASA's Global Ecosystems Dynamics Investigation was launched in December 2018 [17], whilst China's high-resolution Earth observation satellite, Ganfen-7, was launched in November 2019 [18]. The latter two satellites were equipped with full-waveform laser altimeters. Their main missions are forest monitoring and topography surveying, respectively.

Actually, the laser altimeter data with low spatial sampling density cannot generate high-resolution seamless GDEMs. In contrast, they can be used as the Ground Control Points (GCPs)

to validate and calibrate the existing GDEMs [19]–[21]. Rigorous procedures are required to evaluate the geolocation accuracy of laser spots before using them as GCPs. Taking an example of GLAS system, the laser footprints have decimeter-level vertical accuracy (∼13.8 cm), which satisfies the elevation requirement of GCPs in topographic mapping [22], [23]. In contrast, the footprint horizontal coordinates are calculated based on the satellite position, satellite attitude, and distance to the target [24]. Affected by atmospheric refraction and instrument deviation, the horizontal geolocation accuracy of GLAS footprints is only meter level.

The footprint geolocation accuracy is usually validated by *in situ* experiments. In terms of ICESat/GLAS system, Magruder *et al.* [25] captured the real laser locations by placing many electro-optical devices near the satellite reference ground track when the satellite passed in real-time. Although this costly ground-based method is accurate, it is less practical due to limitations in experiment time and place. In cases that on-orbit simultaneous calibration cannot be carried out, several studies attempted to pinpoint the spaceborne LiDAR footprints based on high-resolution Digital Surface Models (DSM) [25]–[27]. For example, Harding *et al.* [26] matched the laser waveforms and DSM elevation data by simulating the LiDAR waveforms pixel by pixel. They found that the GLAS footprints in forest areas had horizontal offsets of 10–30 m. Zhang *et al.* [27] improved the matching method by introducing the surface reflectivity from the airborne LiDAR intensity data. These studies prove that the DSM-based method is feasible to locate the laser footprints, but it is still necessary to explore the performance and applicability of this method on evaluating the footprint geolocation accuracy over large areas. This would guide the calibration experiment design of full-waveform LiDAR satellites.

Therefore, the primary objective of this study is to practice the DSM-based footprint positioning method over several study sites with various land covers based on the ICESat/GLAS data. The DSM-based method takes into accounts the LiDAR configurations and the spatial and reflectance distributions of objects. Focusing on the objective, there are three specific works carried out in this study: 1) to collect the DSM datasets with various land types and the corresponding GLAS waveforms in different laser campaigns; 2) to locate the most likely footprint position by simulating the returned waveforms based on DSM data and matching them with the GLAS waveforms; and 3) to practice the DSM-based footprint positioning method over large areas with different land covers and various laser campaigns. Based on these works, we analyze the performance and applicability of the DSM-based method on evaluating the footprint horizontal geolocation accuracy of spaceborne full-waveform LiDAR. The limitations and future improvements of the DSM-based method are also briefly discussed.

II. Materials

A. Study Sites

Several study sites with different land covers are selected in this study, where the DSM data and GLAS waveforms are both available. The land types are flat land, mountain, ice sheet, forest, and urban, respectively, which involve most land applications of spaceborne LiDAR [13]. The first three types are regarded as the lands without coverings, whilst the latter two are covered by trees or buildings. Fig. 1 displays the maps of the study sites. More details about the study sites and following experimental datasets are summarized in Table I.

B. Digital Surface Models

The DSMs collected in this study are produced from airborne LiDAR point cloud data. First, the noise points are removed based on local point density statistics. Then the DSMs are generated from the first return points by spatial interpolation algorithm [28]. The spatial resolutions of DSM datasets in the five sites are related to the original LiDAR point density. The geometry accuracies of DSM datasets are verified by field sampling measurements. In addition to airborne LiDAR, high spatial resolution satellites, digital aerial photography, and airborne SAR are common sources of high-resolution DSMs [29], [30]. Specifically, surface height data can be obtained by accurate matching between stereo pixels in passive optical images. The phase data in microwave interferograms can be converted to the surface elevation.

C. GLAS Data

The GLAS system uses a Nd:YAG solid-state pulsed laser as a source to emit the pulse signals in two wavelengths at a frequency of 40 times per second [22]. The 1064-nm near-infrared laser is used to measure the surface elevation. The platform altitude is approximately 600 km and the area of detector telescope is approximately 0.709 m^2. The detector sampling frequency is 1 GHz, representing that the vertical resolution of waveform data is ∼15 cm. The zenith angle is less than 0.5°, nearly on a nadir pointing [31]. The total energy of an emitted pulse in 1064 nm is 72 mJ. The pulse is temporally Gaussian-shaped with a 4-ns full width half maximum. The laser pulse forms a nearly circular footprint, where the laser energy follows 2-D Gaussian distribution, falling to e^{-2} at its edge [32]. The National Snow and Ice Data Center provides 15 types of GLAS products (GLA01–GLA15), of which GLA01, GLA05, and GLA14 in Release V33 are used in this study. GLA01 provides the GLAS full-waveform data. GLA05 contains the footprint shape information, including footprint major axis, eccentricity, and orientation. GLA14 records the footprint geographical coordinates, of which horizontal accuracy is evaluated in this study.

The ICESat/GLAS successfully carried out 19 campaigns from 2003 to 2009, supported by three individually-operated lasers [13]. Laser 1 stopped working in March 2003, Laser 2 stopped in May 2005, and Laser 3 stopped working in October 2008. Laser 2 was restarted again and expired in October 2009. To reduce the errors from data sources, we screen the GLAS data in line with the acquisition times of DSM datasets. Specifically, since the restarted Laser 2 has low sensitivity and accuracy, the GLAS datasets from Laser 3 campaigns are collected. For forest site, we prioritize the GLAS data acquired in summer or autumn to reduce errors caused by seasonal forest changes.

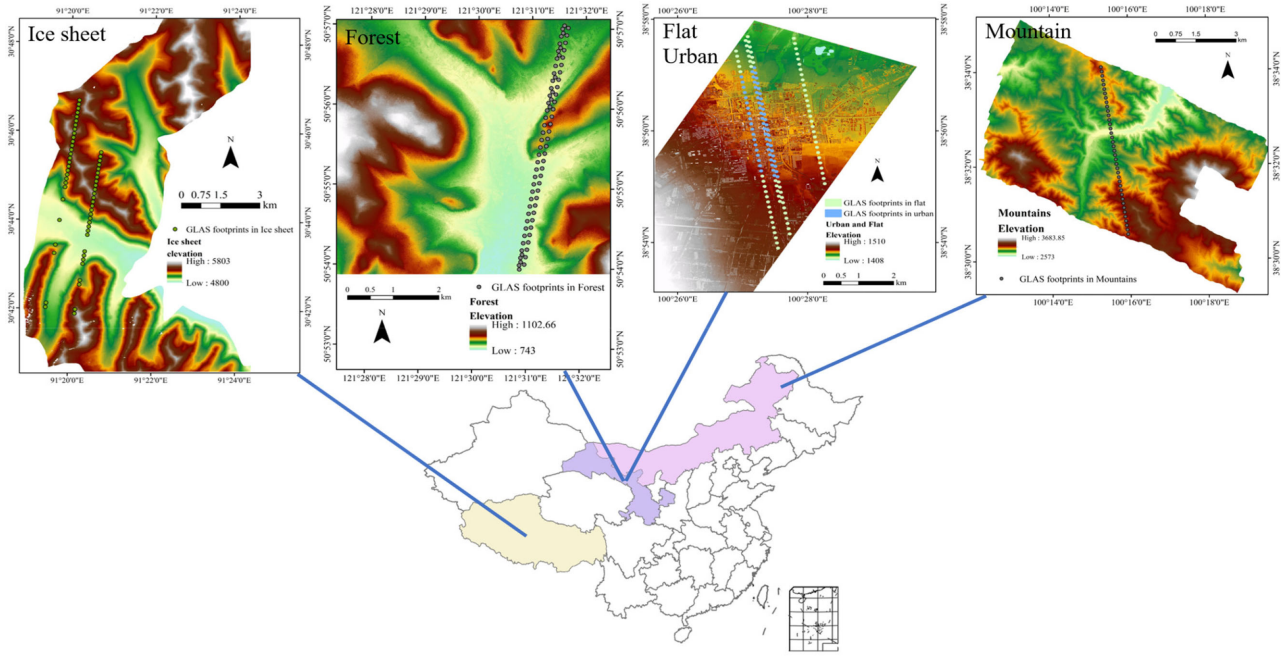

Fig. 1. DSMs and GLAS footprints in the study sites.

TABLE I
SUMMARY OF SITE LOCATIONS, SURFACE FEATURES, COLLECTED GLAS DATASETS, AND DSM DATASETS

Site	1	2	3	4	5
Land cover	Flat	Mountain	Ice sheet	Forest	Urban
Latitude	38°53'-38°58' N	38°30'-38°35' N	30°40'-30°48' N	50°54'-50°58' N	38°53'-38°58' N
Longitude	100°26'-100°30' E	100°12'-100°20' E	91°19'-91°25' E	121°28'-121°32' E	100°26'-100°30' E
Elevation	1408 – 1510 m	2573 – 3684 m	4800 – 5803 m	743 – 1103 m	1408 – 1510 m
Terrain	Low relief	High relief	High relief	Moderate relief	Low relief
Location	Zhangye, Gansu, China	Zhangye, Gansu, China	Naqu, Tibet, China	Genhe, Inner Mongolia, China	Zhangye, Gansu, China
DSM data properties					
Acquisition time	Jul. 2008	Jul. 2012	Aug. 2011	Aug. 2012	Jul. 2008
Acquisition means	Leica ALS70	Leica ALS70	Leica ALS80	Leica ALS60	Leica ALS70
Horizontal accuracy	0.28 m	0.16 m	0.34 m	0.16 m	0.28 m
Vertical accuracy	0.15 m	0.1 m	0.2 m	0.1 m	0.15 m
Spatial resolution	1 m×1 m	0.5 m×0.5 m	2 m×2 m	0.5 m×0.5 m	1 m×1 m
GLAS data properties					
Number of footprints	67	39	56	77	74
Laser campaigns and acquisition times	L3f in Jun. 2006 L3g in Nov. 2006 L3h in Mar. 2007 L3i in Oct. 2007	L3h in Mar. 2007	L3f in Jun. 2006 L3i in Oct. 2007	L3f in Jun. 2006 L3i in Oct. 2007 L3k in Oct. 2008	L3g in Nov. 2006 L3h in Mar. 2007 L3i in Oct. 2007

The annual changes are ignored in this study due to the slow crustal movements in sites 1–3 and the slow growth of natural coniferous forest in site 4. For urban site, no massive urban expansions occurred during the 1- to 2-year time lag between the acquisition dates of GLAS and DSM datasets [33].

III. METHODOLOGY

A. *Framework of DSM-Based Footprint Positioning Method*

The DSM-based footprint positioning method consists of two main steps: waveform simulation and waveform matching. In step 1, we simulate the returned waveform of each possible laser footprint. The simulation model takes into accounts LiDAR configuration, surface spatial distribution, and surface reflectance. Especially, considering that the DSMs might be acquired in different ways, we adopt an image binarization algorithm to generate the reflectance array independent of DSM acquirement ways. In step 2, the simulated waveforms and the GLAS waveform are matched pixel by pixel. The best-match simulated waveform is regarded to be located at the real footprint position. Through these two steps, we locate the footprint center, validate the geolocation accuracy of GLA14 product, and analyze the performance of the DSM-based positioning method. The detailed scheme is shown in Fig. 2.

1) Waveform Simulation: The LiDAR waveform can be regarded as the convolution of the emitted pulse and the response

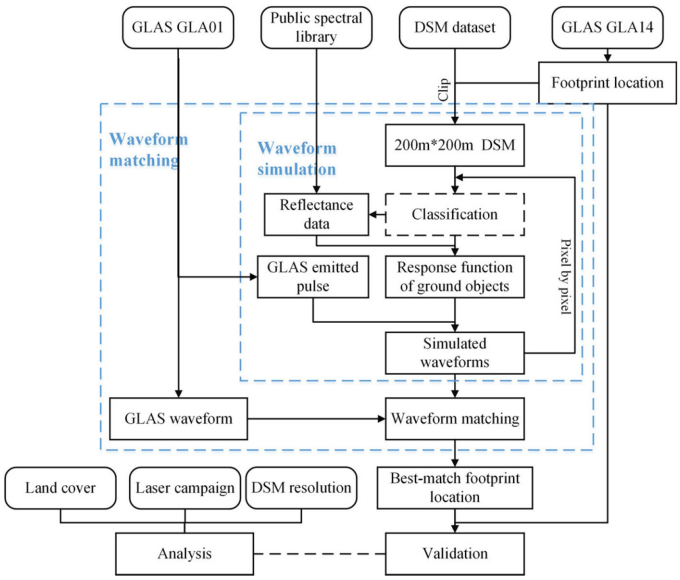

Fig. 2. Schematic diagram of the DSM-based footprint positioning method.

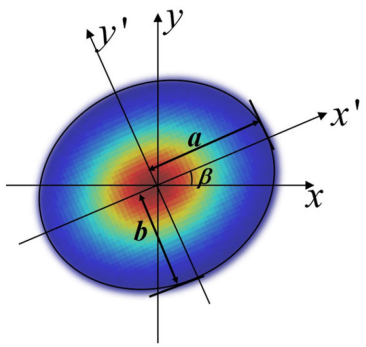

Fig. 3. Spatial distribution of laser energy within an elliptical footprint.

function of ground objects [26], [34]–[36], as in

$$P(t) = \frac{\eta A_R T_{\text{atm}}^2}{hvl^2} \iint \rho(x,y) \cdot h(t) \cdot E(x,y) dxdy * E(t) \tag{1}$$

where η is the integrated efficiency of receiving and photodetection systems, A_R is the detector telescope area, T_{atm} is the laser energy attenuation rate of one-way atmospheric transmission, hv is the energy of a photon, l is the platform altitude, $\rho(x,y)$ is the reflectance distribution function of land surface, $h(t)$ is the height response function of land surface, $E(x,y)$ and $E(t)$ are the time and spatial distribution functions of emitted pulse energy, "$*$" is convolution operation, respectively. In the time domain, the pulse energy is approximate to a 1-D Gaussian distribution, as in (2). In the spatial domain, since the GLAS footprint formed on the ground is not strictly circular but more like an ellipse [22], the spatial distribution of laser energy following a 2-D Gaussian function is determined by the footprint semimajor and semiminor axes, as in (3). Considering the footprint orientation, the footprint coordinate system $x' - y'$ is transformed into the coordinate system $x - y$ of the DSM image, as shown in (4) and Fig. 3

$$E(t) = \frac{E}{\sqrt{2\pi}\sigma} \exp\left(-\frac{t^2}{2\sigma^2}\right) \tag{2}$$

$$E(x',y') = \frac{2E(t)}{\pi ab} \exp\left[-2 \cdot \left(\frac{x'^2}{a^2} + \frac{y'^2}{b^2}\right)\right] \tag{3}$$

$$\begin{bmatrix} x \\ y \end{bmatrix} = \begin{vmatrix} \cos\beta & \sin\beta \\ -\sin\beta & \cos\beta \end{vmatrix} \begin{bmatrix} x' \\ y' \end{bmatrix} \tag{4}$$

$$e^2 = \frac{a^2 - b^2}{a^2} \tag{5}$$

where E is the total energy of an emitted pulse, σ is the pulse width, a is the semimajor axis, b is the semiminor axis, e is the footprint eccentricity, β is the intersection angle between the footprint orientation and the azimuth of DSM image.

The height response function of land surface is related to the surface elevation. When only considering single scattering, it can be calculated from the surface height data in the DSM, as in

$$h(t) = \iint z(x,y) dxdy \tag{6}$$

$$t = \frac{2l}{c} + \frac{x^2 + y^2}{cl} - \frac{2z(x,y)}{c} \tag{7}$$

where $z(x,y)$ is the surface elevation at the position (x,y), t is the one-way laser travel time. The second term in (7) is the time delay caused by the phase front curvature of the diverging laser beam, which can be neglected for spaceborne LiDAR.

For the ground without objects (e.g., flat, mountain, ice sheet, etc.), the surface is assumed to have a uniform reflectivity. For the areas with objects (e.g., forest, urban, etc.), land classification is required. In this study, we assume that the object types in the forest and urban areas are single. This means that the DSM needs to be classified into two categories, objects and ground. Niblack algorithm, an image local binarization algorithm, is performed to segment the objects from the ground [37]. For the central pixel (x,y), the binarized segmentation threshold T is determined on the mean m and variance s of elevations in the corresponding domain range centered on the pixel, as in

$$T(x,y) = m(x,y) + k \cdot s(x,y) \tag{8}$$

where k is an adjustment parameter. Inappropriate value of k would cause the images to be over-segmented or under-segmented. In this study, k is set as -0.02 to ensure that the low vegetation is separated from the ground. The domain range of each pixel is set as 15×15 m based on the usual sizes of trees and buildings. After autoclassifying the objects and ground, their respective reflectances are assigned by user-defined or public spectral libraries. The resulting reflectance array $\rho(x,y)$ has the same location and spatial resolution as the DSM elevation data.

2) Waveform Matching: First, for each footprint, a 200×200 m DSM imagery centered on the GLA14 footprint coordinates is extracted from the DSM dataset. Next, waveform simulation

is conducted pixel by pixel. In order to make the simulated waveforms comparable to the GLAS waveform, they are normalized to the same intensity axes and vertically matched by aligning the location of the maximal waveform intensity. Finally, Pearson's correlation coefficient ρ is calculated between each simulated waveform $S(t)$ and GLAS waveform $R(t)$ to evaluate the similarity of curves [38], as in

$$\rho = \frac{\mathrm{cov}(S(t), R(t))}{\sigma_{S(t)}\sigma_{R(t)}} \tag{9}$$

where cov is the covariance of two curves, σ is the variance. The simulated waveform with the maximal Pearson's correlation coefficient is considered to be located at the most likely footprint position. The footprint shifting on the ground is calculated as the distance between the most likely footprint center and GLA14 coordinate.

B. Evaluation of Footprint Geolocation Accuracy

In this study, the GLAS footprint centers are located using the DSM-based method across the five study sites. To ensure the reliability of final footprint geolocation accuracy, some intermediate results are evaluated. For forest and urban sites covered by objects, the classification results between objects and ground is verified by manual sampling interpretation. The proportion of correctly classified samples to the total samples is used to assess the overall classification accuracy in these two sites.

Next, the simulated waveform in the GLA14 position is compared with the denoised GLAS waveform to verify the validity of waveform simulation model. The simulation accuracy is assessed by Pearson's correlation coefficient and root-mean-square error (RMSE).

Finally, the GLA14 footprint coordinate is compared to the most likely footprint center with the maximal matching similarity. The magnitude and azimuth of the footprint shifting are used to evaluate the accuracy of horizontal geolocations in the GLA14 product. More analyses of footprint geolocation results are done by visualizing the heat map of Pearson's coefficients.

C. Applicability Analysis of DSM-Based Method

To assess the applicability and performance of the DSM-based footprint positioning method, we compare the footprint geolocation shiftings over various land covers and different laser campaigns. The average value and standard deviation of shifting magnitudes and azimuths are calculated in different groups. Also, to explore the impact of DSM data quality on geolocation accuracy evaluation, the method is performed on the same sites with different spatial resolution DSMs.

IV. Results and Discussion

A. Results of Waveform Simulation and Matching

The results of autoclassification are assessed in site 4 and site 5. For the urban area, the overall classification accuracy is 98.8%, ensuring the respective reflectance assignments of ground and buildings. For the forest area, the overall classification accuracy is 96.2%. The misclassification occurs mainly in the low shrub and grass.

Then the simulated waveforms in GLA14 coordinates are compared with the denoised GLAS waveforms of 313 footprints. The average Pearson's correlation coefficient of 313 pairs of waveforms is 0.884, and the average RMSE is 0.00127. The simulation bias is partly due to the inaccurate footprint geolocation, and partly due to the inaccurate simulation model.

The waveform matching is conducted in 313 DSM images corresponding to 313 GLAS waveforms. The GLAS footprints have a 13.63-m average shifting with an 8.37-m standard deviation. The simulated waveforms in best-match footprint positions have higher average Pearson's coefficient (0.934) and lower average RMSE (0.00107) than those in GLA14 positions. However, it is noted that some on-orbit measurements indicates that the footprint geolocation accuracy of GLA14 product is $\sim$4.5 m [22]. The difference of geolocation accuracy from the DSM-based method and the *in situ* measurement is partly related to the inapplicability of DSM-based method and partly caused by the errors of input data sources. Hence, to make better use of the DSM-based positioning method, we separately analyze the footprint geolocation accuracy derived by the DSM-based method over different land covers in Section *B*.

In addition, since 313 footprints are collected from different laser campaigns, the mean and standard deviation of shifting azimuth are meaningless. The footprint geolocation accuracy of different laser campaigns should be separately discussed, as shown in Section *C*.

B. Footprint Geolocation Accuracy Over Different Land Covers

Table II shows the footprint positioning results over the five sites with various land covers. Since the dataset used in each site covers different laser campaigns, the azimuths of footprint shifting are not discussed. Figs. 4 and 5 show some typical examples in five types of land covers, respectively.

For the flat land, there is a high average position shifting magnitude (21.2 m) and a high standard deviation (13.9 m), far from the footprint geolocation accuracy of on-orbit measurements. Taking the example in Fig. 4(a), the simulated waveform in flat land is shaped as a unimodal waveform with narrow pulse width. The GLAS waveform and the simulated waveforms mainly differ in the leading edge, which is likely related to the low grass over the ground. In terms of matching results, although there is a large positioning shifting (28.3 m) between the best-match and GLA14 footprint centers, the Pearson's coefficients of the two simulated waveforms are very close ($\rho = 0.993$ in best-match position, $\rho = 0.992$ in GLA14 position). Based on the heat map, we found that over 80% of the DSM region has very high Pearson's coefficients ($>$0.96). This is related to the extremely high spatial similarity of flat land. Hence, we cannot directly regard the best-match location as the real footprint location. The DSM-based method is not suitable for flat land, so the results of footprint geolocation accuracy are unreliable.

Compared with the flat land, the position shifting in the high-relief mountain and ice sheet areas results in a relatively

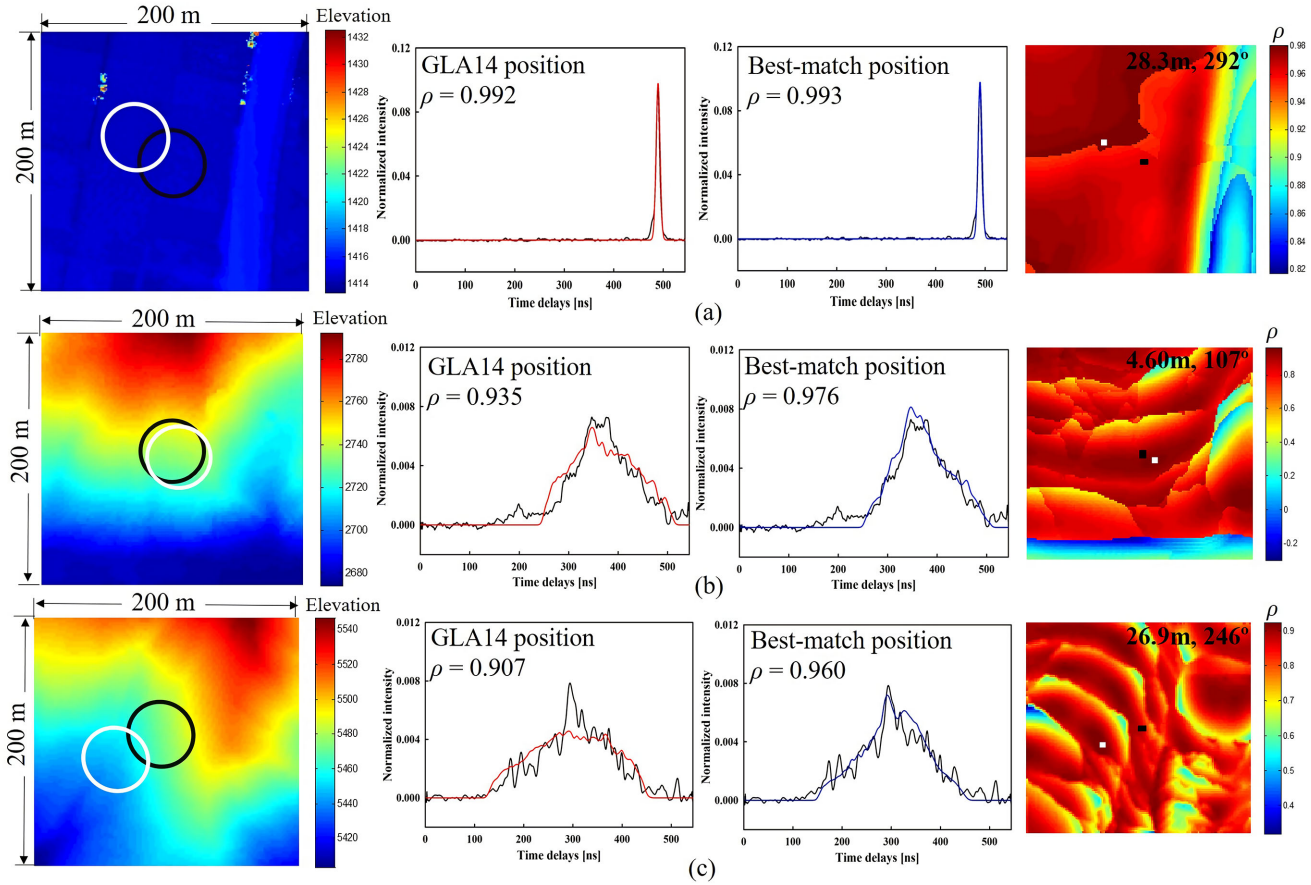

Fig. 4. Examples of footprint positioning in (a) flat land, (b) mountain, and (c) ice sheet. Column 1 shows the 200 × 200 m DSM images around the GLA14 footprint centers, where the black and white ellipses represent the GLA14 footprint and the best-match footprint, respectively. Columns 2 and 3 show the simulated waveform of GLA14 position (red line), the best-match simulated waveform (blue line), and the GLAS waveform (black line), respectively. Column 4 shows the heat map of Pearson's coefficient, where the black and white points are the GLA14 footprint center and the best-match footprint center, respectively. The top right corner of column 4 shows the footprint shifting magnitude and azimuth.

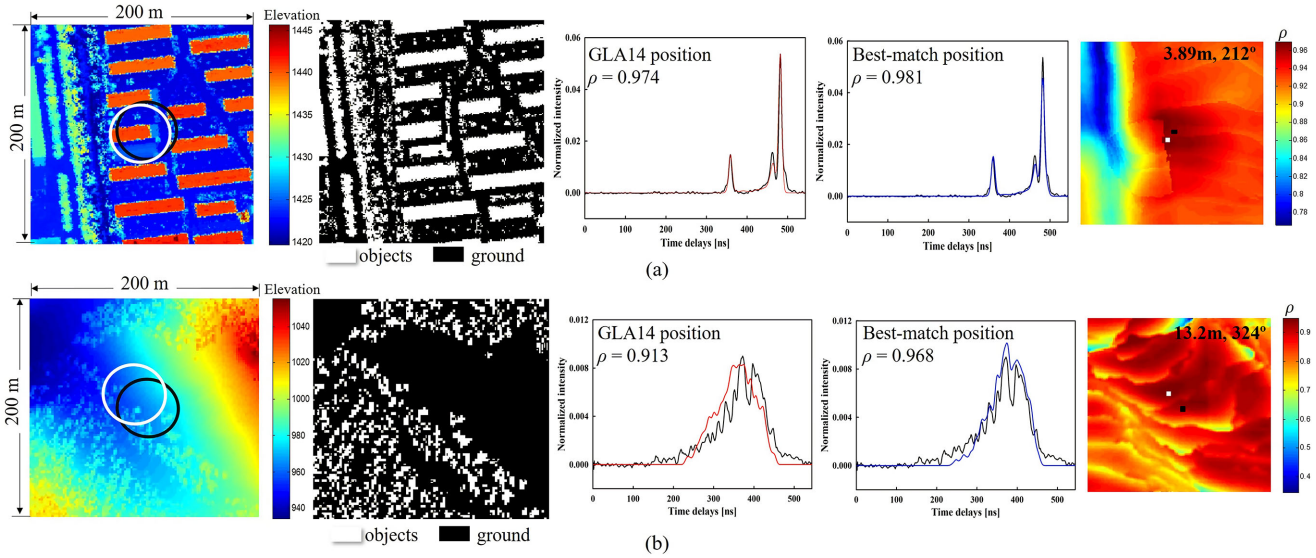

Fig. 5. Examples of footprint positioning in (a) urban and (b) forest. Column 2 shows the classification results of DSM images. The other four columns are the same as those in Fig. 4.

TABLE II
FOOTPRINT GEOLOCATION ACCURACY IN VARIOUS LAND COVERS

	Flat	Mountain	Ice sheet	Forest	Urban	Total
Number of footprints	67	39	56	77	74	313
Average ρ in GLA14 position	0.978	0.845	0.806	0.870	0.935	0.884
Average RMSE in GLA14 position	0.00181	0.000774	0.000854	0.00114	0.00151	0.00127
Average ρ in best-match position	0.989	0.908	0.859	0.920	0.954	0.934
Average RMSE in best-match position	0.00180	0.000567	0.000670	0.000878	0.00117	0.00107
Average shifting magnitude [m]	21.2	16.4	19.2	12.0	8.19	13.63
Standard deviation of shifting magnitude [m]	13.9	8.9	10.8	6.86	4.29	8.37

obvious difference between the GLAS waveform and the simulated waveform in GLA14 location. The simulated waveforms in best-match locations ($\rho_{\mathrm{avg}} = 0.908$ in mountain; $\rho_{\mathrm{avg}} = 0.859$ in ice sheet) are closer to the GLAS waveforms than those in GLA14 locations ($\rho_{\mathrm{avg}} = 0.845$ in mountain; $\rho_{\mathrm{avg}} = 0.806$ in ice sheet). Specifically, as in the examples in Figs. 4(b) and (c), the best-match simulated waveforms have significantly higher Pearson's coefficients than the simulated curves in the GLA14 locations. Based on the DSM images and the heat maps, it is seen that the ice sheet and mountain areas with terrain reliefs have stronger spatial heterogeneity than the flat land. However, it is noted that the returned waveform records the arrangement of relative elevation within the footprint, rather than absolute elevation. We cannot rule out the coincidence that the best-match footprint position has the same vertical distribution, but an elevation difference with the real one. For instance, as in Fig. 4(c), although there is an elevation difference between the best-match real position (white ellipse) and the GLA14 position (black ellipse), almost the same relative elevation distributions make the simulated waveforms similar. Hence, although the waveform similarity is significantly improved in the best-match footprint location, the DSM-based positioning method is still imperfect in mountain and ice sheet areas.

For forest and urban areas, the average shifting magnitudes (12.0 m in forest site and 8.19 m in urban site) are relatively close to the geolocation accuracy of *in situ* measurements. This is related to strong spatial heterogeneity caused by height difference between objects and ground in the forest and urban areas. In these regions, the DSM-based method might be a good way to locate the real footprint center and evaluate the footprint geolocation accuracy. As in the example of Fig. 5(a), regular building structures have explicit height characteristics, thus making the simulated waveform with clear mixture Gaussian shape. The matching result shows that this footprint has a 3.89-m horizontal shifting towards an azimuth angle of 212°. In addition, there is a noticeable difference in the penultimate peak of the best-match simulated waveform and GLAS waveform. This might be caused by the fact that we marked all buildings in the footprint with the same reflectivity.

For the forest site, the canopy grows on the sloping terrain with moderate relief. Due to the overlapping height ranges, the vegetation subwaveform and the ground subwaveform would be mixed. As in the example of Fig. 5(b), the best-match simulated waveform ($\rho = 0.968$) has higher Pearson's coefficient than that in GLA14 position ($\rho = 0.913$). The multipeak locations of best-match waveform are closer to those of GLAS waveform compared to the simulated curve in GLA14 location. The main differences between best-match and real waveforms lie in the leading edge and trailing edge. The difference of leading edge might be related to the inadequate denoising of GLAS waveform. The trailing edge difference might be due to multiple scattering of forest canopy [39] and detector ringing effect [40].

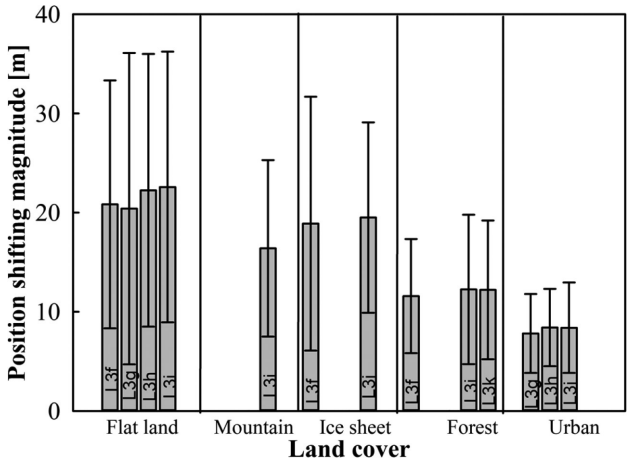

Fig. 6. Position shifting magnitudes during different GLAS laser campaigns.

In fact, the footprint geolocation shifting is caused by atmospheric environment and sensor systematic bias [41], e.g., pointing systematic bias, GPS offset bias, IMU calibration bias, but not related to land surface, etc. The different geolocation accuracies over various land covers indicate the inapplicability of the DSM-based positioning method in areas with few height features. For these sites, putting out the detector arrays on the ground is more reliable to evaluate the footprint geolocation accuracy.

C. Footprint Geolocation Accuracy During Different Laser Campaigns

Figs. 6 and 7 display the position shifting magnitudes and azimuths during various GLAS laser campaigns. Due to the inapplicability of the DSM-based method in relatively homogeneous sites, high standard deviations of position shifting magnitudes and azimuths are reasonable in flat land, mountain, and ice sheet sites. In contrast, the footprint geolocation accuracy results in forest and urban sites deserve more attention. In terms of these two group datasets, we found that the positioning shifting slightly increases with the sensor usage time. The little increment demonstrates that Laser 3 was operating normally and acceptably. Previous research showed that the GLAS waveform quality gradually declines with the sensor running time [42]. The increasing position shifting might be due to the inaccurate laser pointing or be from the positioning error caused by low-quality

TABLE III
FOOTPRINT GEOLOCATION ACCURACY BASED ON DSMS WITH DIFFERENT SPATIAL RESOLUTIONS

Land type	DSM spatial resolution	Average ρ in GLA14 position	Average ρ in best-match position	Average shifting magnitude [m]	Standard deviation of shifting magnitude [m]
Forest	0.5 m	0.870	0.920	12.0	6.86
	1 m	0.867	0.905	12.4	6.91
	2 m	0.841	0.861	13.2	7.41
	4 m	0.783	0.801	15.9	9.21
Urban	1 m	0.935	0.954	8.19	4.29
	2 m	0.921	0.941	8.93	4.53
	4 m	0.873	0.896	11.06	6.02

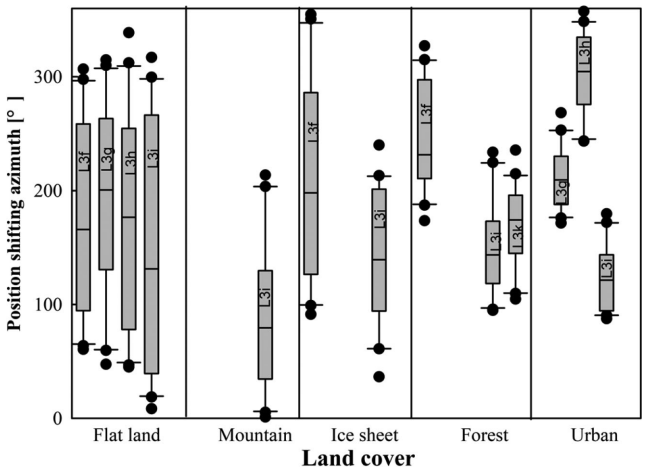

Fig. 7. Position shifting azimuths during different GLAS laser campaigns.

waveforms. Additionally, as in Fig. 7, it is seen that different laser campaigns hold various position shifting azimuths. The footprints on the same track have close shifting azimuths. The waveform data in L3i campaigns are collected both in forest and urban sites. It is seen that the footprints in L3i campaigns are offset to southeast.

In this study, due to the lack of more experimental dataset, we cannot conclude detailed footprint geolocation accuracy during the whole laser campaigns. To evaluate the geolocation accuracy of other lasers, more high-resolution DSM datasets should be collected.

D. Footprint Geolocation Accuracy Based on DSMs With Different Spatial Resolutions

Considering the good performance of the DSM-based method in forest and urban areas, we further explored the effect of DSM spatial resolution on footprint positioning over these two sites. Theoretically, the footprint geolocation accuracy is independent of the spatial resolution of the used DSMs. However, the input DSM datasets with high spatial resolution would help simulate the waveform accurately. Table III shows the footprint geolocation accuracies using the DSMs with different spatial resolutions. Results indicate that as the DSM resolution goes down, the average Pearson's coefficients in both GLA14 and best-match locations decrease, whilst the position shiftings increase gradually. When the DSM is resampled to a 4-m spatial grid, the difference of average position shifting and standard deviation exceeds the difference between grid units. In contrast, the position shifting changes less than one grid unit when using the DSM with 2 m. This suggests that for footprint with ∼50-m diameter, the DSM data with over 2-m spatial resolution is necessary to evaluate the geolocation accuracy.

E. Limitations of DSM-Based Footprint Positioning Method

Although some previous studies have implemented the DSM-based method to locate the so-called real laser footprint, the experiments in this study demonstrate that this method only performs well in the land scene with significant height features. The applicability of the DSM-based method can be explained by the phenomenon "different objects return the same waveform," which is caused by uncertainty of spatial distributions and spectral characteristics. Specifically, it is impossible to derive an unique land scene from the LiDAR waveform without accurate prior knowledge of spatial distributions and spectral properties. Even if these accurate prior data are obtained, only when the land scene is extremely heterogeneous, can the DSM-based method accurately pinpoint the laser footprint. The phenomenon "different objects return the same waveform" and the spatial similarity of land surface are root causes which limit the applicability of DSM-based method. In addition, the positioning results are related to the following error sources, which are not considered in the DSM-based method.

First source is inaccurate land scene. We used the high-resolution DSM to describe the land scene around the laser footprint. However, the DSM data only records the maximal height in the grid, but not the detailed 3-D structures of ground objects. This means that all the objects in a grid are simplified as an opaque surface. Especially in the forest areas, non-rigid leaves are randomly distributed within the crowns in reality. The DSMs cannot provide the details, such as leaf distribution and understory terrain. The simplification of DSM data causes multiple scattering between forest and understory not being considered, thus reducing the accuracy of waveform simulation and increasing the uncertainty of footprint positioning. Additionally, this study uses representative spectral data from public spectral library. In practice, the same objects might hold different spectrums. Inaccurate reflectance assignments might cause waveform misalignments, which also brings uncertainty to footprint positioning.

Second, the best-match footprint position might be not the real one. In the absence of the real position, the DSM-based method regards the position with maximal Pearson's coefficient as the real position. However, affected by the spatial correlation, the Pearson's coefficient might change very little when moving one pixel. Both height errors of DSM data and background noise of full-waveform data might affect the best-match result. The

DSM-based positioning method is sensitive to the quality of input datasets. How to better determine the real footprint position from the matching results should be further discussed.

Based on above error analyses, several suggestions for future improvements of the DSM-based footprint positioning method are described as follows:

1) to determine the most likely footprint position by considering the shifting of adjacent footprints;
2) to determine whether the positioning results are reliable by quantifying the spatial heterogeneity of land surface;
3) to conduct accurate simulations based on accurate land scenes and accurate simulation model.

V. Conclusion

This study practices the DSM-based waveform simulation and matching method to evaluate the footprint horizontal geolocation accuracy of ICESat/GLAS system. The experiments are conducted over several study sites with various land cover and different laser campaigns to explore the applicability and performance of the DSM-based method. Regardless of the experiment differences, the results show that the footprint horizontal coordinates provided by GLAS.V33 products have a 13.98-m average position shifting with an 8.73-m standard deviation, obviously higher than that *in situ* measurements ($\sim$4.5 m). This is related to the fact that the DSM-based positioning method is only suitable for areas with significant height features, but not applicable in areas with high spatial correlation. The derived geolocation accuracy (8.19-m horizontal shifting with 4.19-m standard deviation) is relatively reliable in urban site with relatively high spatial heterogeneity. In addition, it is found that the footprint position shifting slightly increases with the GLAS laser usage time. For the footprint with $\sim$50-m diameter, the DSM with 2-m spatial resolution is necessary to evaluate the footprint geolocation accuracy. These conclusions are helpful to design the calibration experiments of spaceborne full-waveform LiDAR. For example, China's GaoFen-7 satellite is equipped with an optical stereo camera, which can provide high-resolution DSMs for locating the footprints of laser altimeter. Our next work is to develop a rigorous screening procedure of laser footprint based on the geolocation accuracy and other indicators. After that, a global GCP database will be established for topography monitoring and mapping.

Acknowledgment

The authors would like to thank Dong Li, Shezhou Luo, Haiming Qin, Pu Wang, Sheng Nie, Zhenlong Duan, Haole Wang, Qihan Li, and Zhenting Ma for their help in airborne LiDAR measurements and DSM collections. The authors also thank the National Snow and Ice Data Center and the United States Geological Survey for providing free GLAS data and public spectral libraries.

References

[1] P. Passalacqua *et al.*, "Analyzing high resolution topography for advancing the understanding of mass and energy transfer through landscapes: A review," *Earth-Sci. Rev.*, vol. 148, pp. 174–193, 2015.

[2] X. Yang, C. Wang, S. Nie, X. Xi, Z. Hu, and H. Qin, "Application and validation of a model for terrain slope estimation using space-borne LiDAR waveform data," *Remote Sens.*, vol. 10, no. 11, 2018, Art. no. 1691.

[3] Y. Zhang, "Global tectonic and climatic control of mean elevation of continents, and phanerozoic sea level change," *Earth Planetary Sci. Lett.*, vol. 237, no. 3-4, pp. 524–531, 2005.

[4] H. Frey and F. Paul, "On the suitability of the SRTM DEM and ASTER GDEM for the compilation of topographic parameters in glacier inventories," *Int. J. Appl. Earth Observation Geoinformation*, vol. 18, pp. 480–490, 2012.

[5] T. Tadono *et al.*, "Generation of the 30 m-mesh global digital surface model by alos prism," *Int. Archives Photogrammetry, Remote Sens. Spatial Inf. Sci.*, vol. XLI-B4, pp. 157–162, 2016.

[6] M. Zink *et al.*, "TanDEM-X: The new global DEM takes shape," *IEEE Geosci. Rem. Sens. Mag.*, vol. 2, no. 2, pp. 8–23, 2014.

[7] M. Crosetto, "Calibration and validation of SAR interferometry for DEM generation," *ISPRS J. Photogrammetry Rem. Sens.*, vol. 57, no. 3, pp. 213–227, 2002.

[8] P. Reinartz, P. D'Angelo, T. Krauß, D. Poli, K. Jacobsen, and G. Buyuksalih, "Benchmarking and quality analysis of DEM generated from high and very high resolution optical stereo satellite data," *in Proc. Int. Archives Photogrammetry, Rem. Sens. Spatial Inf. Sci.: [2010 Can. Geomatics Conf. Symp. Commission I, ISPRS Convergence Geomatics-Shaping Canada's Competitive Landscape]*, vol. 38, 2010, Art. no. Nr. Part 1.

[9] J. C. F. Diaz, W. E. Carter, R. L. Shrestha, and C. L. Glennie, "LiDAR Remote Sensing," *Handbook of Satellite Applications*. New York, NY, USA: Springer, pp. 757–808, 2016, doi: 10.1007/978-1-4614-6423-5_44-3.

[10] P. Dong and Q. Chen, LiDAR *Remote Sensing* and *Applications*. Boca Raton, FL, USA: CRC Press, 2017.

[11] B. Schwarz, "LIDAR: Mapping the world in 3D," *Nat. Photonics*, vol. 4, no. 7, pp. 429–430, 2010.

[12] A. Swatantran, H. Tang, T. Barrett, P. DeCola, and R. Dubayah, "Rapid, high-resolution forest structure and terrain mapping over large areas using single photon Lidar," *Scientific Rep. UK*, vol. 6, 2016, Art. no. 28277.

[13] X. Wang, X. Cheng, P. Gong, H. Huang, Z. Li, and X. Li, "Earth science applications of ICESat/GLAS: A review," *Int. J. Remote Sens.*, vol. 32, no. 23, pp. 8837–8864, 2011.

[14] H. Zwally *et al.*, "ICESat's laser measurements of polar ice, atmosphere, ocean, and land," *J. Geodynamics*, vol. 34, no. 3-4, pp. 405–445, 2002.

[15] C. Mallet and F. Bretar, "Full-waveform topographic Lidar: State-of-the-art," *ISPRS J. Photogrammetry Rem. Sens.*, vol. 64, no. 1, pp. 1–16, 2009.

[16] T. Markus *et al.*, "The ice, cloud, and land elevation satellite-2 (ICESat-2): Science requirements, concept, and implementation," *Remote Sens. Environ.*, vol. 190, pp. 260–273, 2017.

[17] D. B. Coyle, P. R. Stysley, D. Poulios, G. B. Clarke, and R. B. Kay, "Laser transmitter development for NASA's global ecosystem dynamics investigation (GEDI) Lidar," in *Proc. Lidar Remote Sens. Environmental Monitoring XV*, vol. 9612, 2015, Art. no. 961208.

[18] Z. Hu, *Gaofen-7 satellite was successfully launched, 2019*. [Online]. Available: www.mod.gov.cn/topnews/2019-11/03/content_4854380.htm.

[19] Y. Su, Q. Guo, Q. Ma, and W. Li, "SRTM DEM correction in vegetated mountain areas through the integration of spaceborne LiDAR, airborne LiDAR, and optical imagery," *Remote Sens.*, vol. 7, no. 9, pp. 11202–11225, 2015.

[20] L. Yue, H. Shen, L. Zhang, X. Zheng, F. Zhang, and Q. Yuan, "High-quality seamless DEM generation blending SRTM-1, ASTER GDEM v2 and ICESat/GLAS observations," *ISPRS J. Photogrammetry Remote Sens.*, vol. 123, pp. 20–34, 2017.

[21] F. Satgé *et al.*, "Accuracy assessment of SRTM v4 and ASTER GDEM v2 over the Altiplano watershed using ICESat/GLAS data," *Int. J. Remote Sens.*, vol. 36, no. 2, pp. 465–488, 2015.

[22] J. B. Abshire *et al.*, "Geoscience Laser Altimeter System (GLAS) on the ICESat mission: On-orbit measurement performance," *Geophysical Res. Lett.*, vol. 32, no. 21, 2005, Art. no. L21S02.

[23] C. A. Shuman *et al.*, "ICESat Antarctic elevation data: Preliminary precision and accuracy assessment," *Geophysical Res. Lett.*, vol. 33, no. 7, 2006, Art. no. L07501.

[24] L. A. Magruder, C. E. Webb, T. J. Urban, E. C. Silverberg, and B. E. Schutz, "ICESat altimetry data product verification at White Sands Space Harbor," *IEEE Trans. Geosci. Remote Sens.*, vol. 45, no. 1, pp. 147–155, 2006.

[25] Y. Chunyu, X. Kun, and B. Yunfei, "A matching method of spaceborne laser altimeter big footprint waveform and terrain based on cross cumulative residual entropy," *Acta Geodaetica et Cartographica Sinica*, vol. 46, no. 3, pp. 346–352, 2017.

[26] D. J. Harding and C. C. Carabajal, "ICESat waveform measurements of within-footprint topographic relief and vegetation vertical structure," *Geophys. Res. Lett.*, vol. 32, no. 21, 2005, Art. no. L21S10.
[27] W. Zhang, S. Li, Z. Zhang, R. Liu, and Y. Ma, "Using the waveform matching to precisely locate footprints of a satellite laser altimeter," *Infrared Laser Eng*., vol. 47, no. 11, 2018, Art. no. 1117007.
[28] N. Pfeifer and G. Mandlburger, "LiDAR data filtering and DTM generation," in *Topographic Laser Ranging and Scanning*. Boca Raton, FL, USA: CRC Press, 2017, pp. 307–334.
[29] C. Lemaire, "Aspects of the DSM production with high resolution images," *Int. Archives Photogrammetry, Remote Sens. Spatial Inf. Sci.*, vol. 37, no. B4, pp. 1143–1146, 2008.
[30] C. Magnard, M. Frioud, D. Small, T. Brehm, H. Essen, and E. Meier, "Processing of MEMPHIS Ka-band multibaseline interferometric SAR data: From raw data to digital surface models," *IEEE J-STARS*, vol. 7, no. 7, pp. 2927–2941, 2014.
[31] B. E. Schutz, H. Zwally, C. Shuman, D. Hancock, and J. DiMarzio, "Overview of the ICESat mission," *Geophysical Res. Lett.*, vol. 32, no. 21, 2005, Art. no. L21S01.
[32] W. Yang, W. Ni-Meister, and S. Lee, "Assessment of the impacts of surface topography, off-nadir pointing and vegetation structure on vegetation Lidar waveforms using an extended geometric optical and radiative transfer model," *Remote Sens. Environ.*, vol. 115, no. 11, pp. 2810–2822, 2011.
[33] X. Yang *et al.*, "Extraction of multiple building heights using ICESat/GLAS full-waveform data assisted by optical imagery," *IEEE Geosci. Remote S.*, vol. 16, no. 12, pp. 1914—1918, Dec. 2019.
[34] J. B. Blair and M. A. Hofton, "Modeling laser altimeter return waveforms over complex vegetation using high-resolution elevation data," *Geophysical Res. Lett.*, vol. 26, no. 16, pp. 2509–2512, 1999.
[35] G. Sun and K. J. Ranson, "Modeling Lidar returns from forest canopies," *IEEE Trans. Geosci. Remote Sens.*, vol. 38, no. 6, pp. 2617–2626, 2000.
[36] C. S. Gardner, "Ranging performance of satellite laser altimeters," *IEEE Trans. Geosci. Remote Sens.*, vol. 30, no. 5, pp. 1061—1072, Sep. 1992.
[37] W. Niblack, *An Introduction to Digital Image Processing*. Englewood Cliffs, NJ, USA: Prentice Hall, 1985.
[38] P. Sedgwick, "Pearson's correlation coefficient," *BMJ*, vol. 345, 2012, Art. no. e4483.
[39] X. Yang, C. Wang, and X. Xi, "Multiple scattering effect on forest physiological parameters of multispectral Lidar canopy waveforms," in *Proc. IGARSS 2019–2019 IEEE Int. Geosci. Remote Sens. Symp.*, 2019, pp. 8467–8469.
[40] L. A. Magruder, A. L. Neuenschwander, and S. P. Marmillion, "Lidar waveform stacking techniques for faint ground return extraction," *J. Appl. Remote Sens.*, vol. 4, no. 1, 2010, Art. no. 043501.
[41] S. Luthcke, D. D. Rowlands, J. J. McCarthy, D. E. Pavlis, and E. Stoneking, "Spaceborne laser-altimeter-pointing bias calibration from range residual analysis," *J. Spacecraft Rockets*, vol. 37, no. 3, pp. 374–384, 2000.
[42] S. Nie, C. Wang, G. Li, F. Pan, X. Xi, and S. Luo, "Signal-to-noise ratio–based quality assessment method for ICESat/GLAS waveform data," *Opt. Eng.*, vol. 53, no. 10, 2014, Art. no. 103104.

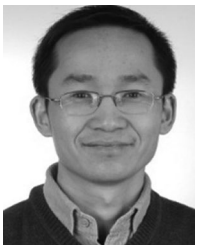

Cheng Wang received the Ph.D. degree in remote sensing from the Université Louis Pasteur (ULP), Strasbourg, France, in 2005.

He is currently a Professor with the Aerospace Information Research Institute, Chinese Academy of Sciences, Beijing, China. His research interests include LiDAR remote sensing mechanisms and multimode LiDAR data processing.

Xuebo Yang received the B.E. degree in remote sensing science and technology from the Wuhan University, Wuhan, China, in 2016. She is currently working toward the Ph.D. degree at the Aerospace Information Research Institute, Chinese Academy of Sciences, Beijing, China.

Her research interests include the sensor design and land applications of spaceborne full-waveform LiDAR.

Xiaohuan Xi received the M.S. degree in environmental geography from the Peking University, Beijing, China, in 2000.

She is currently an Associate Professor with the Aerospace Information Research Institute, Chinese Academy of Sciences, Beijing, China. Her research interests include LiDAR radiative transfer modeling and forest characteristics estimations.

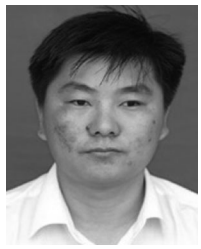

Hebing Zhang received the Ph.D. degree in photogrammetry and remote sensing from the Henan Polytechnic University, Jiaozuo, China, in 2015.

He is currently a Professor with the College of Surveying and Land Information Engineering, Henan Polytechnic University, Jiaozuo, China. His research interests include topography surveying and mapping using remote sensing techniques.

Shichao Chen received the B.E. degree in surveying engineering from the Henan Polytechnic University, Jiaozuo, China, in 2015. He is currently working toward the Ph.D. degree at the College of Geoscience and Surveying Engineering, China University of Mining and Technology, Beijing, China.

His research interests include 3-D scene reconstruction using LiDAR data.

Shuwen Peng received her B.E. degree in remote sensing science and technology from the Wuhan University, Wuhan, China, in 2018. She is currently working toward the master's degree at the Aerospace Information Research Institute, Chinese Academy of Sciences, Beijing, China.

Her research interests include data processing and classification of airborne LiDAR point cloud.

Xiaoxiao Zhu received the B.E. degree in remote sensing science and technology from the Wuhan University, Wuhan, China, in 2016. She is working toward the Ph.D. degree at the Aerospace Information Research Institute, Chinese Academy of Sciences, Beijing, China.

Her research interests include data processing and vegetation application of spaceborne LiDAR.